ELSEVIER

Contents lists available at ScienceDirect

Journal of Alloys and Compounds

journal homepage: www.elsevier.com/locate/jalcom



Role of intermediate phases on microstructures, wear and corrosion resistance in new-developed ($\alpha + \beta$) titanium alloy

Bo Song ^{a,b,*}, Yanwei Xue ^a, Junjie Ni ^a, Wenlong Xiao ^{b,c,**}, Junshuai Wang ^b, Chaoli Ma ^{b,c}, Lian Zhou ^b, Hui Chen ^a

- ^a School of Materials Science and Engineering, Liaocheng University, Liaocheng 252059, China
- b Key Laboratory of Aerospace Advanced Materials and Performance of Ministry of Education, School of Materials Science and Engineering, Beihang University, Beijing 100191 China
- ^c Tianmushan Laboratory, Xixi Octagon City, Yuhang District, Hangzhou 310023, China

ARTICLE INFO

Keywords: Titanium alloy Intermediate phases α precipitation Wear resistance Corrosion resistance

ABSTRACT

A new $(\alpha+\beta)$ Ti alloy has been designed and prepared in this work, and the results show that three intermediate phases will be transformed including α'' martensite, O' and ω . Upon continuous heating, the α'' martensite decomposes gradually and disappears before α precipitation. The ω and O' domains are generated continuously upon aging, and such two intermediate phases co-exist when α phase nucleation occurs. It has been proved that the ω and O' domains play a direct role in promoting α phase formation. Through the ω and O' domains assisting α nucleation mechanism, a uniform distribution of fine α precipitates can be obtained after aging. Under the treatment of pre-aging at 300 °C plus aging at 600 °C, the α phase having smallest size and largest number density is obtained, resulting in highest wear resistance and corrosion resistance. For this sample, its average friction coefficient and wear ratio are 0.174 and 3.75×10^{-4} mm³/(N·m), respectively. During friction tests, the mixture of abrasive wear, adhesive wear and oxidation wear should be activated. Due to the formation of passivation films on the alloy surface, this alloy has exhibited better anti-corrosion properties than Ti-6Al-4 V alloy, and its corrosion current density in 3.5 wt% NaCl solution can be reduced to 1.79×10^{-8} A·cm⁻². Compared with the samples under duplex aging treatments, the direct aged sample also presents outstanding anti-corrosion properties.

1. Introduction

Titanium alloy has been widely used in aerospace and defense fields due to its low density, outstanding formability and excellent corrosion resistance [1]. These properties are primarily attributed to the distribution of fine α precipitates within β matrix, and the features of α play a significant role, i.e. morphology, size, volume fraction and distribution. Numerous efforts have been made on optimizing the α phase features so far via tailoring alloy chemical compositions and heat treatment parameters. It is known that obviously refined microstructures can be obtained in Ti alloy by intermediate phases assisting α nucleation mechanisms, as well as desirable mechanical properties [2–4]. However, the influence of intermediate phases on α nucleation and growth still remains unclear, resulting in great difficulties on controlling alloy

compositions and heat treatment parameters via intermediate phases assisted $\boldsymbol{\alpha}$ nucleation mechanisms.

Generally, duplex aging treatment and slow heating to aging temperatures are utilized to develop intermediate phases before α precipitation [5,6]. One opinion argues that the α phase inclines to nucleate at the interfaces between intermediate phases and β , and intermediate phases act as precursors providing more favorable nucleation sites for α transformation. The energy barrier for α nucleation at the interfaces can also be apparently reduced [7]. While the other researchers discuss that the α -stabilizers enriched regions associated with intermediate phases formation are more likely serve as preferential nucleation sites for α phase, such as O-rich [8] or Al-rich [9] regions. This is due to that the α precipitation requires solute redistribution upon aging. The origin of such difference is that the underlying mechanisms of intermediate

E-mail addresses: songbolcu@163.com (B. Song), wlxiao@buaa.edu.cn (W. Xiao).

^{*} Corresponding author at: School of Materials Science and Engineering, Liaocheng University, Liaocheng 252059, China.

^{**} Corresponding author at: Key Laboratory of Aerospace Advanced Materials and Performance of Ministry of Education, School of Materials Science and Engineering, Beihang University, Beijing 100191, China.

phases assisting a nucleation are unrevealed. Many studies have evidenced the refinement of microstructures and improvement of mechanical properties by intermediate phases contribution, including α'' [10], ω [6], O' [11], O" [12] and β' [13]. Superfine α precipitates are reported to be obtained in Ti-5553 alloy by non-conventional transformation pathway, mediated by ω precipitates [14]. The influences of ω on α precipitation has been evaluated on two aspects involving coherency stress field and locally compositional variations, and the result shows the contributions of such two aspects are identical based on atom probe tomography technique and first-principles density functional theory calculations. When two or three kinds of intermediate phases are developed simultaneously in alloy, they may co-exit and play a more complicit role on affecting α precipitation [15]. This can obviously reduce the sensitivity of microstructures and properties to heating rate to aging temperatures, being more suitable to manufacture structures with large thickness. The transformation between different intermediate phases has also been found in literature depending on alloy composition and phase transformation kinetics, like $\alpha'' \leftrightarrow \omega$ [16], $\alpha' \leftrightarrow O'$ [17], $\alpha'' \leftrightarrow O'$ [18] and O" \leftrightarrow O' [19]. Therefore, it is necessary to study the α nucleation and growth behavior in alloy consisting a variety of intermediate phases. Generally, a uniform distribution of fine α is beneficial to mechanical properties of Ti alloy, while the corrosion resistance may be deteriorated since microcell corrosion prefers to take place at β/α interfaces. Li et al. [20] found that the Ti-3Al-6Cr-1Fe alloy obtained higher strength than the other components, and it exhibited obviously lower corrosion resistance. However, S.R.A. Zaree et al. [21] argues that a homogenous dispersion of fine α phase is beneficial to obtain better corrosion resistance. Achieving a good balance of mechanical properties and corrosion resistance has attracted great attentions now, and more efforts need to be made to reveal the underlying mechanisms. The demand for Ti alloys as orthopedic implant materials in biomedical field is significantly increasing in recent years, their corrosion behavior and wear performance are often evaluated simultaneously [22-24].

In this work, a new Ti alloy has been developed, in which three kinds of intermediate phases will be formed during continuous heating. By changing heat treatment parameters, the influence of three intermediate phases on α nucleation is studied. It is found that refined microstructures and good comprehensive properties can be obtained, attributing to these intermediate phases.

2. Materials and methods

2.1. Alloy preparation and microstructures observation

A new $(\alpha + \beta)$ titanium alloy, Ti-5 Nb-3Mo-3 V-3Al-2Zr-1Fe (wt%, Ti-533321) is prepared by arc melted in argon atmosphere protection, using Ti, Al, Nb, Mo, V, Zr and Fe with 99.99 % purity. The Ingot has been re-melted five times to ensure chemical homogeneity. Then, the ingots are hot-rolled at 800 °C with thickness reduction of 80 %. The detailed chemical composition of Ti-533321 alloy has been given in Table 1, and its [Mo] is calculated to be 7.9 % based on the formula of $[Mo] = Mo + 0.67 \times V + 0.44 \times W + 0.28 \times Nb + 0.22 \times Ta + 2.9 \times Fe$ + 1.6 \times Cr - Al (wt%). The average bonding order (Bo) and molecular dorbital energy value (Md) of this alloy is 2.79 and 2.40, respectively. delectron theory has been reported to be an effective method of designing Ti alloys, in which Bo and Md are two important parameters. The Bo is the bond order that is a measure of the covalent bond strength between Ti and an alloying element. The Md is d-orbital energy level between Ti and an alloying transition metal, which correlates well with the electronegativity and the radius of the element. The values for pure elements

Table 1The detailed chemical composition of Ti-533321 alloy.

		•			•			
Elements	Ti	Nb	Mo	V	Al	Zr	Fe	[Mo]
wt%	Bal.	4.71	3.59	3.27	2.72	2.39	1.34	7.9

in bcc Ti have been listed in literature [25]. The average values of bonding order (Bo) and molecular d-orbital energy value (Md) of this alloy are calculated by the equations of $\overline{B}_o = \sum_{i=1}^n x_i(B_o)_i$ and $\overline{M}_d = \sum_{i=1}^n x_i(M_d)_i$. The β transus temperature of this alloy has been measured to be 820 ± 5 °C by metallographic method.

In this work, the samples are cut from the hot-rolled alloy, and firstly solution treated at 850 $^{\circ}\text{C}$ for 0.5 h followed by water quenching. For the duplex heat treatments, the samples are pre-aged at 200 $^{\circ}$ C, 300 $^{\circ}$ C and 400 °C isothermally holding for 1 h and water quenched, and then aged at 600 °C for 8 h. To compare with that, some samples are directly aged at 600 °C for 8 h, referred as RT in this paper. The microstructures are revealed by Kroll's reagent (10 ml HF + 30 ml HNO₃ + 70 ml H₂O), and observed by optical microscope (OM), scanning electron microscope (SEM) and transmission electron microscope (TEM). TEM and highresolved TEM (HRTEM) observations were performed on a JEM-2100 F with an accelerating voltage of 200 kV, and the TEM samples are prepared by FIB technique. The preparation of TEM samples has been showed in Supplementary Fig. S1. Differential scanning calorimetry (DSC) measurement is conducted on Netzsch STA449F3 calorimeter using specimens of 20 mg at heating rate of 10 °C/min. The phase constituents in samples are analyzed by X-ray diffraction (XRD). To identify the transformation of intermediate phases, selected are electron diffraction (SAED) analysis is employed. The thickness, length and number density of α precipitates in aged samples are measured by Image-Pro-Plus software.

2.2. Friction tests and electrochemical tests

After aging at 600 °C, the microhardness of samples are evaluated at a load of 9.8 N for 10 s. Ten points are tested for each sample to get the average value and error. The wear resistance of aged samples is obtained by friction tests under dry sliding condition, conducted on MFT-EC4000. The friction tests are conducted at room temperature in air using stainless steel ball. The scratch length, applied load, fixed sliding velocity, frequency and sliding time are 5 mm, 2 N, 0.02 m/s, 2 Hz and 10 min, respectively. The wear ratio of samples is calculated by W=V/ $(F \cdot L)$, in which V is the wear volume loss, L the total sliding distance and F the applied load. The Polarization curves and corresponding electrochemical impedance spectroscopy (EIS) are obtained by CHI660E electrochemical workstation. The aged samples are working electrode, and saturated calomel works as reference electrode and Pt counter electrode. All electrochemical tests are performed at room temperature in 3.5 wt% NaCl aqueous solutions. The open-circuit potential for each test is monitored for 30 min to allow the working electrode to a steady state, and the potentiodynamic polarizations are obtained with a scan rate of 1 mV/s. The Bode impedance and phase diagrams are measured in the frequency range from 10⁵ Hz to 10⁻² Hz with a signal amplitude perturbation of 10 mV. All electrochemical tests are performed three times. After friction or corrosion tests, the sample surface is observed by SEM observations equipped with EDS analysis section. The corrosion products are examined by X-ray photoelectron spectrometer (XPS, ESCALAB250xi).

3. Results

3.1. Intermediate phases transformation

Fig. 1a shows the location of Ti-533321 alloy in *Bo-Md* diagram [25], and it is thought that this alloy has a comparably low stability, belonging to $(\alpha + \beta)$ type alloy. The Bo-Md diagram is an effective tool to evaluate the stability of Ti alloy. It means that the microstructural stability of Ti alloys during deformation. Generally, it is utilized to suspect the deformation mechanisms of alloy during loading, including slipping, mechanical twinning and stress induced martensitic transformation. With the stability increasing, the controlling deformation mechanism

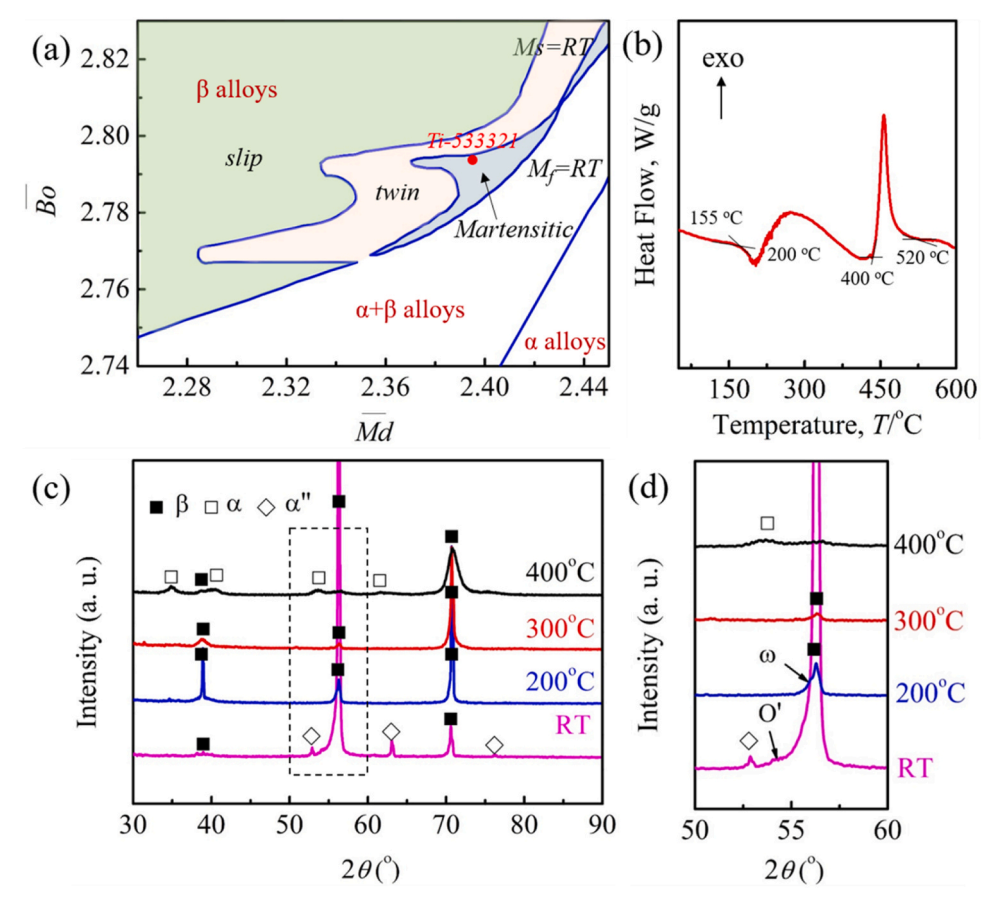


Fig. 1. The location of Ti-533321 alloy in phase stability diagram (a), and (b) heat flow of β -quenched sample during heating at 10 °C/min. (c) XRD results showing phase constituents of samples aged at different temperatures, and (d) detailed view in the interval enclosed by the dashed line.

changes as the sequence of stress induced martensitic transformation, mechanical twinning and dislocations slipping. When solution treated above β transus temperature followed by water quenching, plenty of α'' martensite plates can be observed. Based on EDS analysis, there is a uniform distribution of various elements (shown in Supplementary Fig. S2), i.e. Ti, V, Al, Nb, Mo, Zr and Fe. During continuous heating obvious endothermic and exothermic peaks caused by phases precipitation and decomposition are noted (Fig. 1b). It is observed that a small endothermic reaction occurs from 155 °C to 200 °C, which should be resulted by the α'' martensite decomposition. Then, apparent exothermic peak from 200 °C to 400 °C caused by intermediate phases formation appears. The exothermic peak at 400 $^{\circ}C$ \sim 520 $^{\circ}C$ is thought due to α phase precipitation. This indicates that intermediate phases transformation occurs before the α precipitation, which offers us opportunity to tailor α precipitates via intermediate phases influencing nucleation and growth behavior.

When the β -quenched sample is isothermally aged at various temperatures for 1 h, the phase constituents are analyzed by XRD technique shown in Fig. 1c. For the β -quenched sample, obvious α'' martensite peaks are visible, as well as the retained β matrix diffraction peaks. It means that the microstructure of the β -quenched sample consists of α'' martensite and retained β matrix. After aging at 200 °C, the diffraction peaks of α'' martensite disappear, and only β phase peaks are visible. It is suspected that during aging at 200 °C, the α'' martensite decomposes completely. When increases the pre-aging temperature to 300 °C, only β phase diffraction peaks are observed. It is difficult to distinguish diffraction peaks of intermediate phases by XRD analysis. When preaged at 400 °C, α phase diffraction peaks with very low intensity are observed in addition to β peaks. It is suggested that during aging at 400 °C the α phase precipitation occurs, being according with the DSC

result. In the close-up view of XRD pattern in the dashed lines in Fig. 1c, some intermediate phases with extremely low intensity can be found. Reflections coming from O' phase are also noted in the β-quenched sample, and ω phase diffraction peak may be presented in the sample pre-aged at 200 °C (Fig. 1d). To evidence the formation of intermediate phases, TEM observations are conducted and showed in the following paragraph. The microstructures of samples pre-aged at different temperatures are observed and given in Fig. 2. It is corresponding with the XRD results, and plenty of α'' martensite presents in the β -quenched sample shown in Fig. 2a. For the sample pre-aged at 200 °C, these α'' martensite dissolves, and equiaxed β grains are obtained (Fig. 2b). This evidences that the endothermic reaction at 155 $^{\circ}C$ \sim 200 $^{\circ}C$ is indeed caused by α'' martensite decomposition. For the sample pre-aged at 300 °C, there is no α precipitates appear shown in Fig. 2c. The presence of α phase can be observed until the pre-aging temperature increasing up to 400 °C as arrowed in Fig. 2d, being according with DSC result above.

The bright-field (BF) TEM micrograph showing microstructure of the β -quenched sample is given in Fig. 3a, in which plenty of α'' martensite needles are observed. Within the β grains, the SAED pattern (the inset in Fig. 3a) recorded along $[113]_{\beta}$ direction shows apparent reflections coming from intermediate phases. It is thought that the reflections located at 1/3 and $2/3(2\overline{1}1)_{\beta}$ positions belong to athermal ω , and the reflections located at $1/2(2\overline{1}1)_{\beta}$ position come from O' phase. It is known that the ω phase is formed by $(111)_{\beta}[111]_{\beta}$ collapse mechanism [26], and the O' is developed by $(110)_{\beta}[110]_{\beta}$ shuffle process [27]. The formation of these intermediate phases, including α'' martensite, ω and O', indicates again the instability of β Ti-533321 alloy. These intermediate phases are thought to be transformed upon quenching from solution temperature, and should not involve solute atoms diffusion. For the α'' martensite, detailed TEM observations are conducted shown in Fig. 3b,

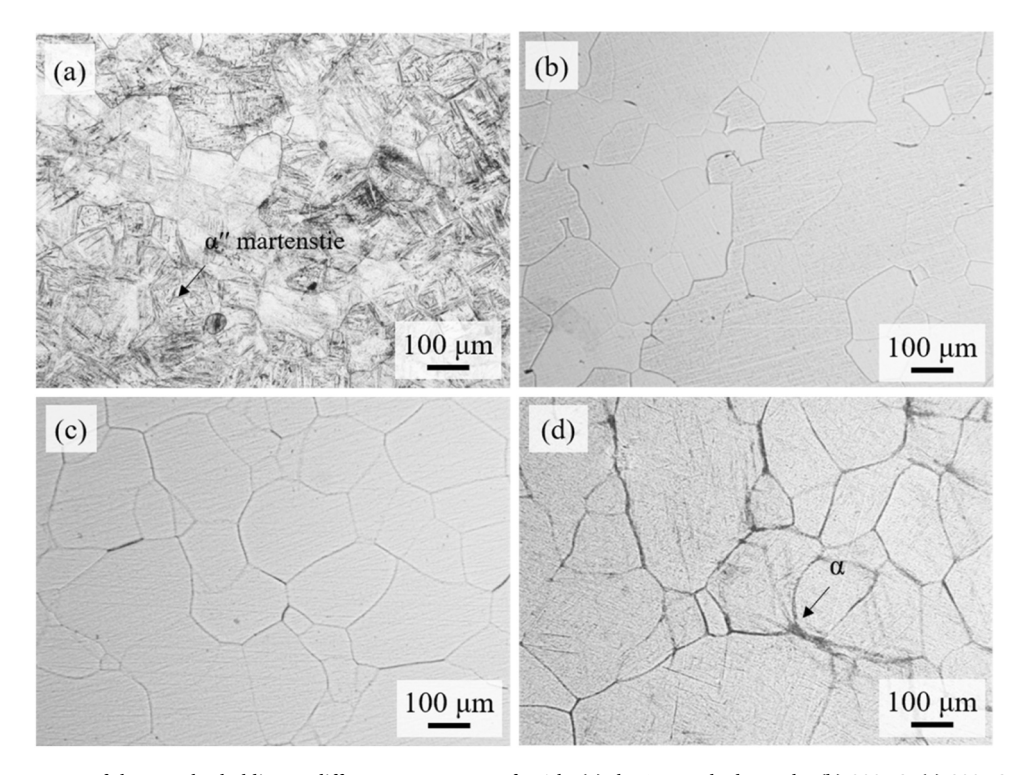


Fig. 2. Microstructures of the samples holding at different temperatures for 1 h, (a) the β quenched sample, (b) 200 °C, (c) 300 °C and (d) 400 °C.

in which apparent α'' phase reflections are noted in the inset SAED pattern along [113]₆ direction. In titanium alloy, there are two types of α'' phase have been reported in literature, α'' martensite and isothermal α'' . The α'' martensite are thought to be developed by $\{112\}_{B}[111]_{B}$ shear process followed by $(110)_{\beta}[110]_{\beta}$ shuffle, and the isothermal α'' phase is formed by displacive and diffusive mixed process. During continuous heating, the α'' martensite may dissolve into β matrix and/or transform into O', ω phases, depending on alloy composition and phase transformation kinetics. The orientation of α'' martensite in the β -quenched sample is also studied, which should be $[113]_{6}\{110\}_{6}$ // $[112]_{6}$ // $[111]_{6}$. In addition, some other intermediate phases are also found within grains. By selecting the circled reflections in Fig. 3a, the dark-field (DF) TEM images showing the distributions of athermal ω and O' domains are obtained (Fig. 3(c, d)). It is found that both ω and O' domains are uniformly distributed in alloy, and the O' domains seem to have smaller average diameter than the athermal ω. The average diameter of O' domains is measured to be 1.5 nm, and it is 2.7 nm for the $\ensuremath{\omega}$. Since the reflections of O' and α'' phases sometimes locate at the same positions, it is necessary to distinguish such two intermediate phases. As the O' is formed by $(110)_{\beta}[110]_{\beta}$ shuffle, and the α'' is formed by $\{112\}_{\beta}[111]_{\beta}$ shear plus $(110)_{\beta}[110]_{\beta}$ shuffle processes, the degree of $\{112\}_{\beta}[111]_{\beta}$ shear can be employed to identify the nature of intermediate phases [18]. It should be zero for the O' phase, and not zero for α'' . The SAED pattern viewed along [001]6 direction (Fig. 3e) is used to study the shear degree of $\{112\}_{\beta}$ planes along $[111]_{\beta}$ direction. The diffraction intensity along the blue and red dash lines are recorded shown in Fig. 3f, and it is found that such shear degree is zero because of x = y. As a result, the nature of such intermediate phase is identified as O', not α'' .

It has been argued that α'' martensite has dissolved after aging above 200 °C based on OM observations and XRD analysis, but the evolution of athermal ω and O' phases during low-temperature aging is also need to be investigated in detail. The microstructure of sample pre-aged at 300 °C are investigated by TEM observations shown in Fig. 4. Plenty of nano-scaled intermediate phases are visible embedding on β matrix (Fig. 4a), and obvious reflections of isothermal ω and O' phases are noted in the SAED pattern along $[011]_{\beta}$ direction. Combined DF TEM image

showing the uniform distribution of such two intermediate phases is given in Fig. 4b, in which the number density of intermediate phases is obviously larger than that in β -quenched one. The ω and O' phases are highlighted by blue and red contrast, respectively. This indicates that the ω and O' nano-domains are continuously developed during aging at 300 °C. The exothermic peak from 200 °C to 400 °C in DSC curve are indeed caused by the $\boldsymbol{\omega}$ and O' precipitation. Separated DF TEM micrographs exhibiting the ω and O' domains are presented in Fig. 4c and Fig. 4d, respectively. It has been discussed in literature that the formation of O' may be associated with ω formation. The transformation of isothermal ω can actually facilitate O' phase development, and the close spatial proximity between ω and O' domains has been found. Upon aging solute atoms, *i.e.* Al, O and Mo et al., are inclined to diffuse outside of ω , leading to local enrichment of solute atoms in regions nearby ω. The Al and/or O atoms enrichment will contribute to the $(110)_{6}[110]_{6}$ shuffle and results in O' formation. Hence, it is suspected that the transformation of isothermal ω can effectively contribute to O' development in the sample aged at 300 °C.

3.2. Microstructures evolution

After pre-aging at low temperatures, the samples are then aged at 600 °C, and the aged microstructures are given in Fig. 5. It is obviously noted that the α precipitates are uniformly distributed in samples, and the average size and number density of α precipitates have been summarized in Table 2. The α precipitates in the sample pre-aged at 300 °C has the smallest thickness of $0.08\pm0.03\,\mu m$, as well as the largest number density of 16 ± 4 laths/ μ m². This indicates that the sample preaged at 300 °C obtains much finer α precipitates than the other components, and should obtain stronger precipitation hardening effect. The grain boundary α phase in this sample is more likely discontinuous shown in Fig. 5c, which further indicate more effective nucleation sites activation for intergranular α precipitation. For the directly aged sample, the α precipitates have slightly larger average thickness of 0.09 $\pm 0.02 \,\mu\text{m}$, and their number density decreases to $13\pm 2 \, \text{laths/}\mu\text{m}^2$. The average thickness, length and number density of α precipitates in the sample pre-aged at 200 $^{\circ}$ C are $0.11\pm0.05~\mu m,~0.6\pm0.21~\mu m$ and 10 ± 3

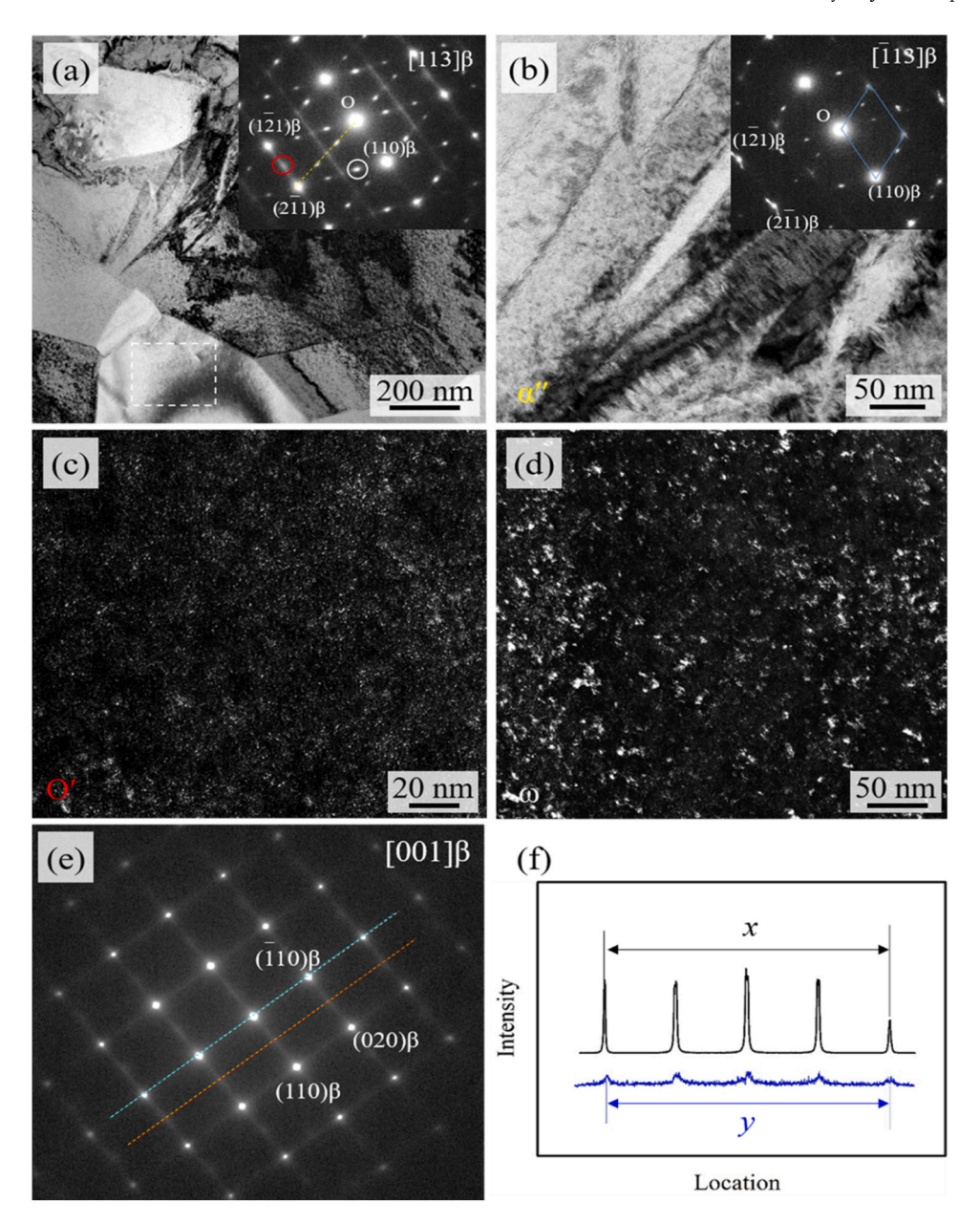


Fig. 3. BFTEM micrographs (a, b) of the solution treated sample and the inset SAED patterns along [113] $_{\beta}$ direction, and (c, d) the distribution of O' and ω phases. (e) SAED pattern recoded along [001] $_{\beta}$ direction and (f) the intensity profile along blue and red lines.

laths/µm², respectively. Although a uniform distribution of fine α precipitates are still visible in the sample pre-aged at 400 °C, their average thickness seems to be the largest, as well as the lowest number density. The thickness, length and number density of α precipitates in the sample pre-aged at 400 °C are measured to be 0.16±0.05 µm, 0.47±0.16 µm and 11±5 laths/µm², respectively. The grain boundary α phase seems to be continuous. It is suspected that the sample pre-aged at 400 °C should have the lowest microhardness and wear resistance.

3.3. Tribological properties

The microhardness of aged samples are showed in Fig. 6, and it is noted that the microhardness increases firstly and then drops greatly with the pre-aging temperature increasing. The sample pre-aged at 300 °C has the largest microhardness of 273 ± 2 HV. This is according with microstructural observations above. The microhardness values of samples pre-aged at 200 °C and 400 °C are 255 ± 3 HV and 250 ± 5 HV, respectively. It deserves to note that the sample directly aged at 600 °C

also obtains acceptable microhardness of 257 ± 6 HV. The wear resistance of these aged samples exhibits similar inclination with the preaging temperature climbing. The friction coefficient curves of aged samples during testing are showed in Fig. 7a, in which the friction coefficient of sample pre-aged at 300 °C is apparently lower than the other components. The average friction coefficient and wear ratio of aged samples are concluded in Fig. 7b, and the sample pre-aged at 300 °C has the lowest wear ratio. The average friction coefficient and wear ratio of this sample are 0.174 and 3.75×10^{-4} mm³/(N·m), respectively. This indicates that the alloy obtains best wear resistance when pre-aged at $300\ ^{\circ}\text{C}$ under duplex aging treatment. It is found that the tribological properties of these aged sample are closely related to their microstructures, and the α precipitates with smaller size and higher number density exhibit obviously stronger aging hardening effect. The directly aged sample and the one pre-aging at 200 °C present comparatively lower microhardness and wear resistance due to the coarser intergranular $\boldsymbol{\alpha}$ precipitates. The average friction coefficient and wear ratio of the sample directly aging at 600 °C are 0.338 and 4.71×10^{-4} mm³/(N·m),

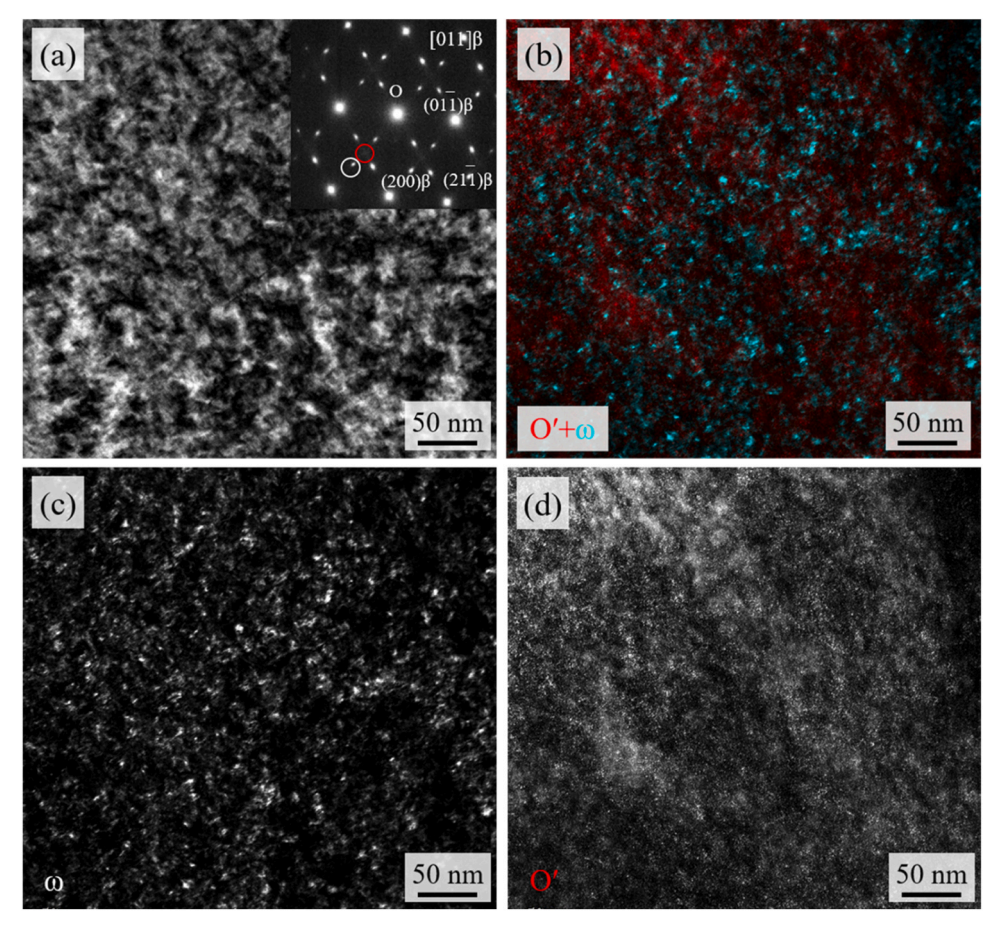


Fig. 4. BFTEM micrograph (a) showing the microstructure of the sample heated to 300 °C with the inset SAED pattern along [011] $_{\beta}$ direction, and (b) the combined DFTEM image showing co-existence of ω and O' domains. (c, d) DFTEM images showing the distribution of ω and O' domains, respectively.

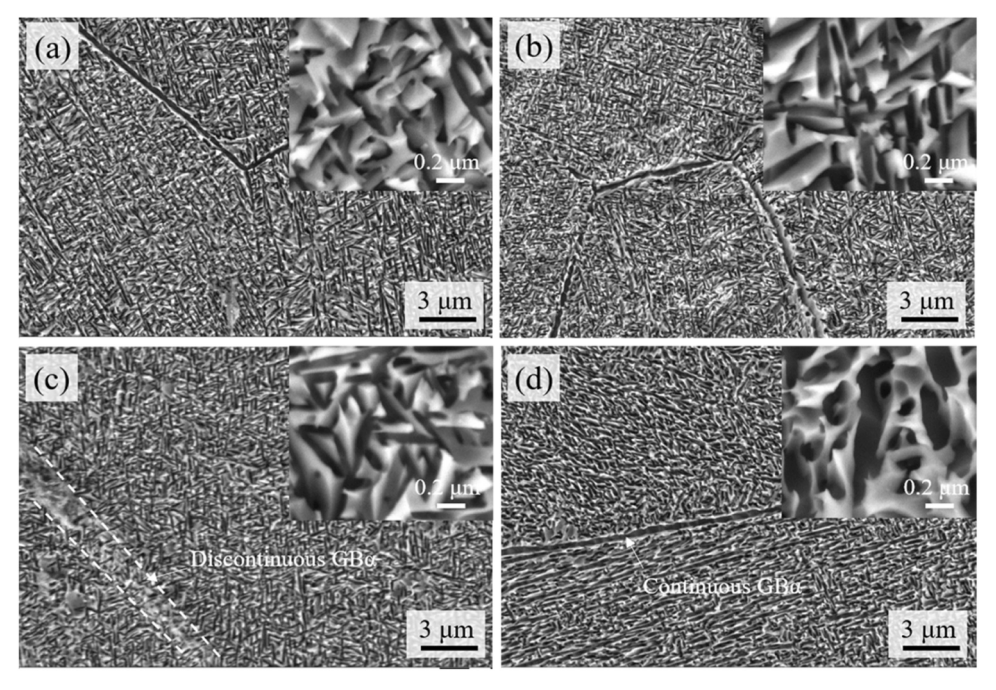


Fig. 5. Microstructures of the samples under dual-age treatments (a) RT, (b) $200\,^{\circ}$ C, (c) $300\,^{\circ}$ C and (d) $400\,^{\circ}$ C.

Table 2 Features of α precipitates in these samples after aging at 600 $^{\circ}\text{C}.$

	Thickness, μm	Length, μm	Aspect ratio	Number density, laths/ μm²
RT	0.09±0.02	0.58 ± 0.11	6.44±0.2	13±2
200 °C	$0.11 {\pm} 0.05$	$0.6 {\pm} 0.21$	5.45 ± 0.4	10 ± 3
300°C	$0.08 {\pm} 0.03$	$0.42{\pm}0.14$	$5.25{\pm}0.16$	16±4
400°C	0.16 ± 0.05	0.47 ± 0.16	$2.94{\pm}0.1$	11 ± 5

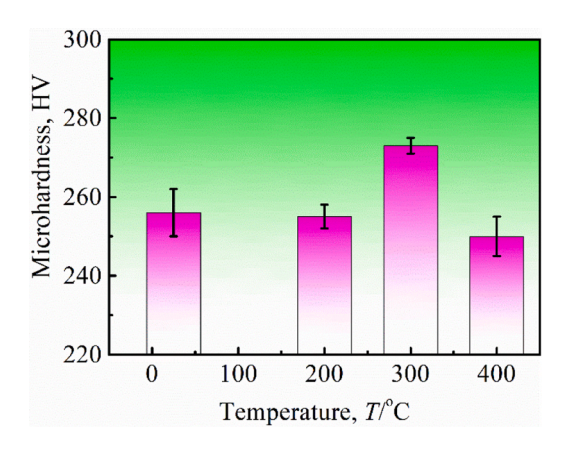


Fig. 6. Microhardness of the samples under dual-age treatments.

respectively. For the sample pre-aged at 200 °C, they are 0.367 and $4.95\times10^{-4}~\text{mm}^3/(\text{N}\cdot\text{m})$, respectively. The largest wear ratio is obtained in the sample pre-aged at 400 °C, which reaches up to $6.04\times10^{-4}~\text{mm}^3/(\text{N}\cdot\text{m})$.

To clarify the wear mechanisms of aged samples during friction tests, the characters of worn surface are carefully studied. It is observed that apparent grooves and wear debris appear on the surface shown in Fig. 8a, which suggests the occurrence of great plastic deformation. The appearance of grooves is the indicative of abrasive wear [28]. Besides, plenty of wear debris are visible, which demonstrates serious exfoliation of alloy, as referred by dash lines in Fig. 8b. It is suspected that these wear debris may be a mixture of alloy and oxides based on XRD analysis (Fig. 8c), in which obvious diffraction peaks belonging to TiO₂ and Al₂O₃ has been identified except for Ti peaks. EDS maps shown in Fig. 8 (d-h) further prove that the nature of such wear debris, including TiO₂, Al₂O₃, Fe₂O₃ and Cr₂O₃. To evidence the formation of these oxides, XPS spectrum of the worn surface is given in Fig. 9. The peaks of TiO₂, Al₂O₃, Fe₂O₃ and Cr₂O₃ are clearly noted. As a result, it is reasonable to suggest that the alloy has been oxidized during friction process, and the oxidation wear mechanism has been activated. In conclusion, it is thought that the wear mechanisms of aged samples during friction tests involve abrasive wear, adhesive wear and oxidation wear.

3.4. Corrosion resistance

The corrosion resistance of aged samples is also investigated in this work, and their corresponding polarization curves are presented in Fig. 10a. The potentiodynamic polarization curves consist of cathodic and anodic polarization branches, and the electrochemical parameters can be obtained from such potentiodynamic polarization curves. These polarization curves shape are similar, inferring that the aged samples exhibit similar electrochemical behavior. Such similarities should be attributed to the formation of thin ${\rm TiO_2}$ films on surface of aged samples. It has been reported that a compact layer will be spontaneously formed as a result of anodic oxidation. The compact oxides layer plays a significant role in increasing corrosion resistance since it can protect physically the alloy from electrolyte ions and prevent dissolution. Based on Tafel slope extrapolation method, the corrosion potential and current density are obtained (Fig. 10b). With the pre-aging temperature increasing, a gradual increment of corrosion potential from -0.374 V to -0.159 V is observed. The increment of corrosion potential with preaging temperature increasing indicates the thermodynamically enhanced stability of aged samples, as well as better anti-corrosion properties. Corrosion current density is also practically used to evaluate the corrosion resistance of alloy. In comparison with the sample pre-aged at 200 °C and 400 °C, the directly aged sample and the one preaged at 300 °C have lower corrosion current density. The corrosion current density of directly aged sample is 1.90×10^{-8} A·cm⁻², and that of the ones pre-aged at 200 °C, 300 °C and 400 °C are 2.01×10^{-8} A·cm⁻², 1.79×10^{-8} A·cm⁻² and 7.50×10^{-6} A·cm⁻², respectively. It is known that lower corrosion current density means the higher corrosion resistance of alloy in 3.5 wt% NaCl solution, and the sample pre-aged at 300 °C should have the best anti-corrosion properties. The alloy under direct aging treatment also obtains comparable corrosion resistance. Compared with such two samples, obviously higher corrosion current density and lower corrosion resistance are found in the other two samples. It has been reported in literature that the corrosion current density of Ti-6Al-4 V alloy in 3.5 wt% NaCl solution is 3×10^{-7} A·cm⁻², therefore the samples pre-aged at 200 °C and 300 °C and the directly aged one exhibit better anti-corrosion properties than Ti-6Al-4 V alloy.

These results above have evidenced that the sample pre-aged at 300 $^{\circ}$ C and the directly aged one have higher corrosion resistance than the other components. SEM images showing the features of corroded surface are showed in Fig. 11. Some corrosion products can be observed on the surface, and the corresponding EDS data shows obvious enrichment of O element and exclusion of Ti and Al atoms. It is suspected that these corrosion products may be the oxides including TiO₂ and/or Al₂O₃. XPS analysis of such corrosion products confirms the existence of TiO₂ and Al₂O₃ shown in Fig. 12. Aiming to study the electrochemical behavior of alloy, EIS experiments are also conducted. Nyquist and Bode diagrams of the aged samples are plotted shown in Fig. 13, and the equivalent circuit model is inserted in Fig. 13a. There is only one capacitive loop from high to low frequencies. R₁ and R₂ refer to the

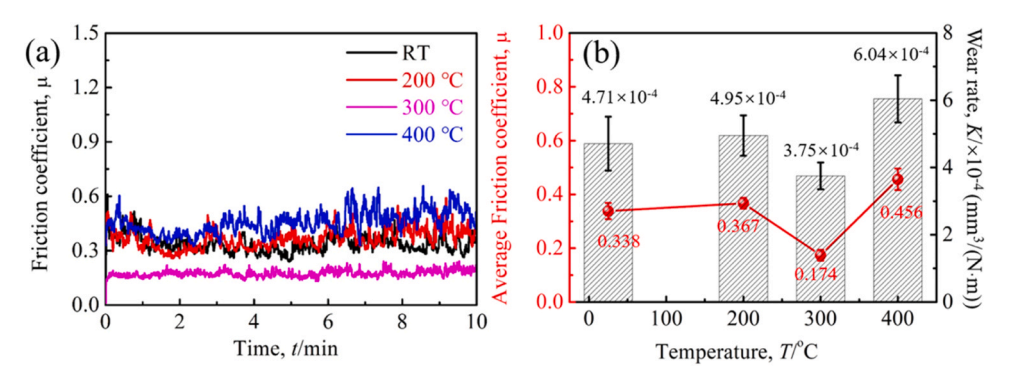


Fig. 7. Friction coefficient curves of the aged samples (a), and (b) the average friction coefficients and wear rates.

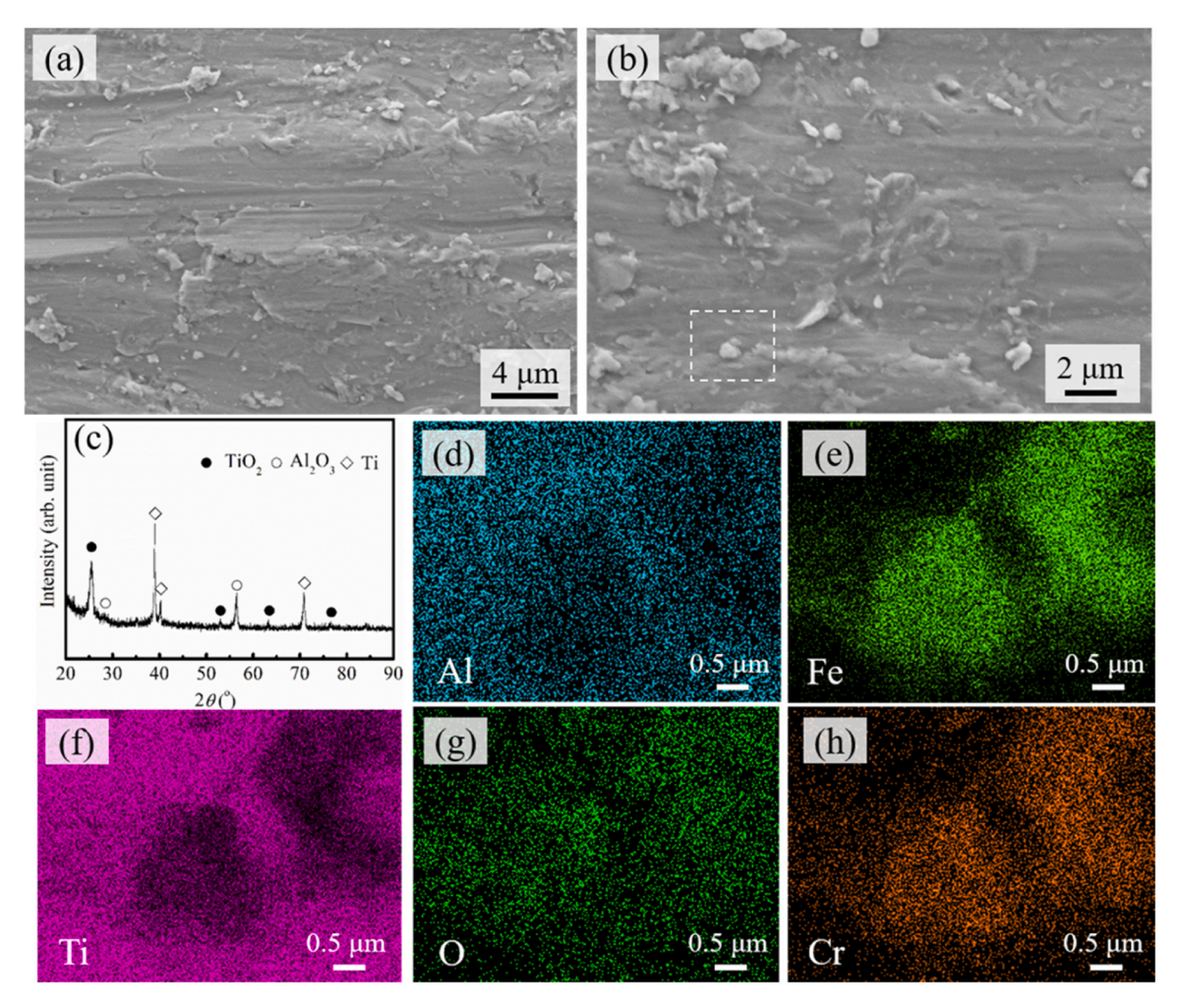


Fig. 8. SEM images (a, b) showing the typical worn surface of the aged samples and (c) XRD analysis of the worn surface. EDS maps (d-h) showing the local concentration of Al, Fe, Ti, O and Cr atoms.

electrolyte resistance and the resistance of passivation films, respectively. CPE1 is a constant associated with the characteristics of passivation films. The resistance of passivation films should be regarded as identical for all aged samples, because it is primarily determined by the surface reactivity, roughness and current distributions et al. R₃ represents the charge transfer resistance in electric double layer structure. Due to the electrolyte resistance R₁ is far smaller than the charge transfers resistance R₃, the electrochemical corrosion reactions are mainly controlled by the charge transfers process in electric double layer structure. As shown in Fig. 13a, the Nyquist diagrams display a semicircular shape, which is similar to other Ti alloys [29]. The diameter of capacitive loop can be employed to deduce the difficulty of electron transferring, so the capacitive loop with a larger diameter indicates a higher corrosion resistance. It is easy to found that the capacitive loop for the sample pre-aged at 300 °C has larger diameter than the directly aged one. Therefore, it is accepted that the sample pre-aged at 300 °C has slightly higher corrosion resistance than the directly aged one. Using ZView software and the equivalent circuit model, the fitted values of R₁, R₂ and R₃ are obtained. The charge transfer resistance R₃ for the directly aged sample is fitted to be $1.13\times10^7 \Omega$, and that is $1.36\times10^7 \Omega$ for the sample pre-aged at 300 °C. The Bode impedance and phase plots are given in Fig. 13b, in which the impedance of sample pre-aged at 300 °C is slightly larger than the directly aged one, also indicating its higher corrosion resistance. Furthermore, there is a platform appears in the middle frequency region on Bode phase curves, implying the formation of compact passivation film on the surface of aged samples [30].

4. Discussion

Based on mentioned results above, it is found that the largest wear resistance and best anti-corrosion properties are achieved in the sample pre-aged at 300 °C. This should be caused by the development of α precipitates with smallest thickness and highest number density. It is well known that stronger precipitation hardening effect will be achieved in alloy with finer α precipitates, resulting in larger microhardness and wear resistance. For the corrosion resistance, it is also found closely associated with the morhphology, size, number density and distribution of α precipitates [20–24]. In this work, the largest corrosion resistance is obtained in the sample pre-aged at 300 $^{\circ}\text{C}$ attributing to the finest α precipitates. It is suggested that a much denser and more compacted passivation film may be formed on the surface of alloy, since the β/α interfaces with larger numbers density facilitate oxygen transmission and contribute to passivation film development. It is observed that a much finer α precipitates are obtained in the 300 °C pre-aged sample than that of 400 °C pre-aged one, as well as larger wear resistance and corrosion resistance. It has been clearly argued that the α precipitation in this alloy are via intermediate phases assisting mechanisms, and the $\boldsymbol{\omega}$ and O' play the direct role in promoting α nucleation. It is reasonable to suspect that the 300 $^{\circ}$ C pre-aged sample has larger α nucleation rate than the 400 °C pre-aged sample. Pre-aging at 400 °C results in the ω and O' dissolution, which can be also deduced by DSC curve (Fig. 1b). The α precipitation takes place at 400 °C, and the intermediate phases ω and O' will dissolve at this temperature.

Due to the properties of alloy are primarily determined by micro-

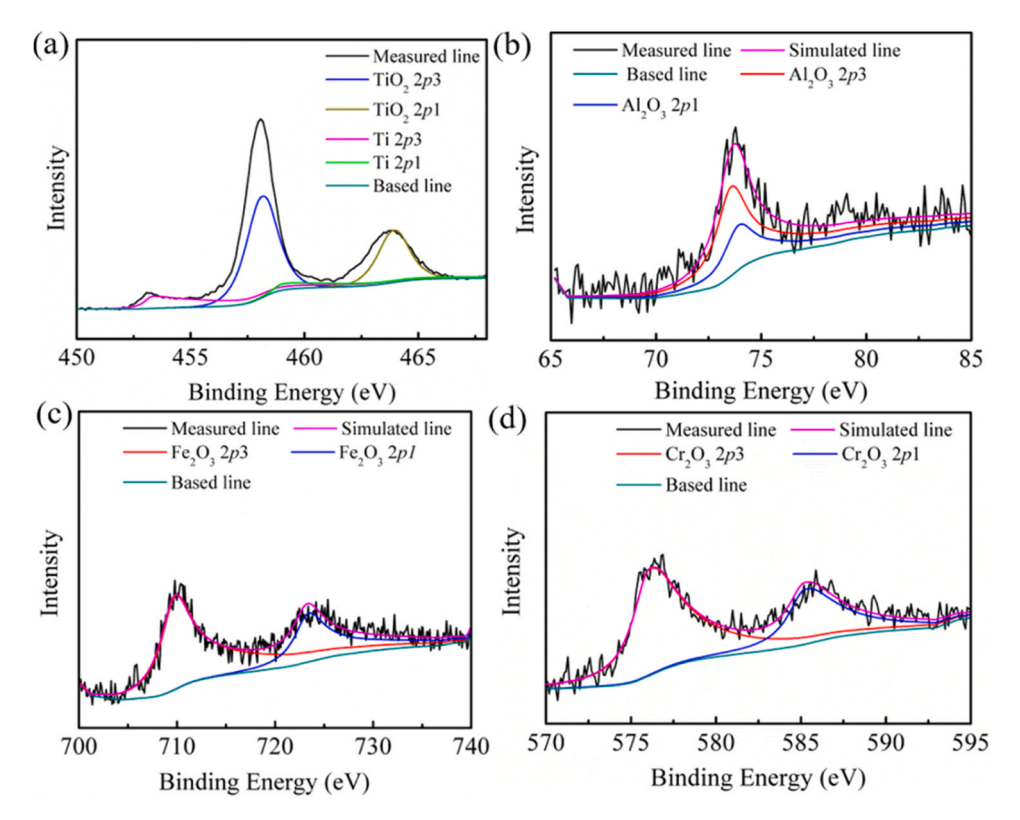


Fig. 9. (a) Ti2p, (b) Al2p, (c) Fe2p and (d) Cr2p XPS spectrum of the worn surface.

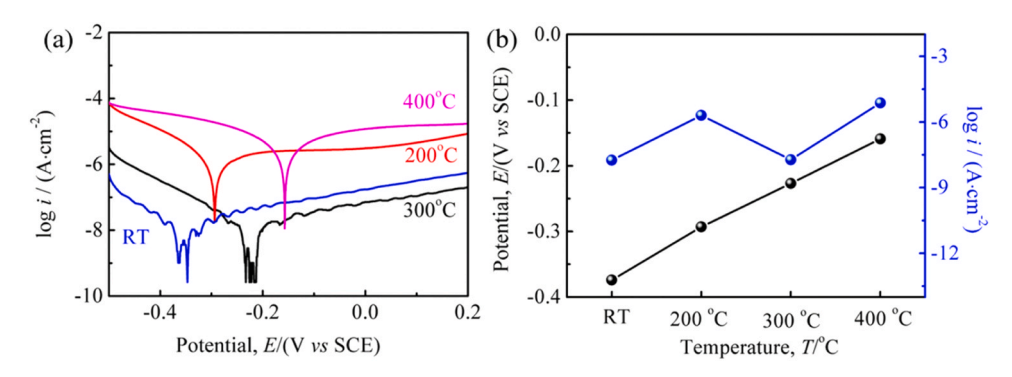


Fig. 10. Polarization curves of the aged samples pre-aged at different temperatures (a), and (b) the corresponding corrosion potential and current density.

structures, it is necessary to explain the nucleation behavior of α phase in Ti-533321 alloy during continuous heating. There are three intermediate phases formation during early aging in alloy, including α'' , O' and ω phases. It has been proved that the α phase begin to precipitate from 400 °C based on the DSC curve (Fig. 1b) and OM observations (Fig. 2). To study the nucleation of α , the β -quenched sample is isothermally holding at 300 °C for 1 h and then directly up-quenched to 400 °C followed by water quenching shown in Fig. 14. In this sample, the α needles appear with very low quantities. The reflections of α at $1/2\{21\overline{1}\}_{\beta}$ location having low intensity is also visible in the SAED pattern along $[113]_{\beta}$ direction. At the same time, we note obvious reflections belonging to ω phase and O'. By selecting the circled reflections, DF TEM image showing the co-existence of ω and O' domains accompanying with α needles are obtained shown in Fig. 14b. This indicates that plenty of ω and O' domains are developed when the α precipitation occurs. It is reasonable to suggest that the nucleation of α may be assisted by such two intermediate phases, ω and O'. Generally, the reflections of O' and α can be observed at the same locations, and the O' phase reflections are also located at $1/2\{21\overline{1}\}_{\beta}$ position. The O' and α can be distinguished by

their morphology, and the α phase exhibits needle-like shape and the O' domains have ellipsoidal shape. Therefore, it is argued that the ω and O' domains play a significant role in promoting α phase formation in Ti-533321 alloy upon aging.

To clearly evidence the influence of such two intermediate phases on α nucleation, HRTEM observations of this sample have been performed (Fig. 15). The close proximity of α needle and ω , O' phases has been confirmed, and the fast Fourier transformed (FFT) patterns corresponding to the regions of I, II and III have been provided. It further evidences that the ω and O' domains can directly promote α precipitation in this alloy during aging treatment. For the α'' martensite, it is thought that the α'' may plays an indirect role in promoting α transformation by affecting ω and O' domains development. During continuous heating, the decomposition of α'' occur. It may transform back into β matrix, or evolve into O' and/or ω . Pere Barriobero-Vila et al. [31] have tracked α'' martensite decomposition during heating by fast in situ high energy synchrotron X-ray diffraction, and they found the continuous transformation of $\alpha'' \to \beta$. Besides, the evolution between α'' and O' has also been observed in Ti-24 Nb-4Zr-8Sn alloy during loading and/or cooling

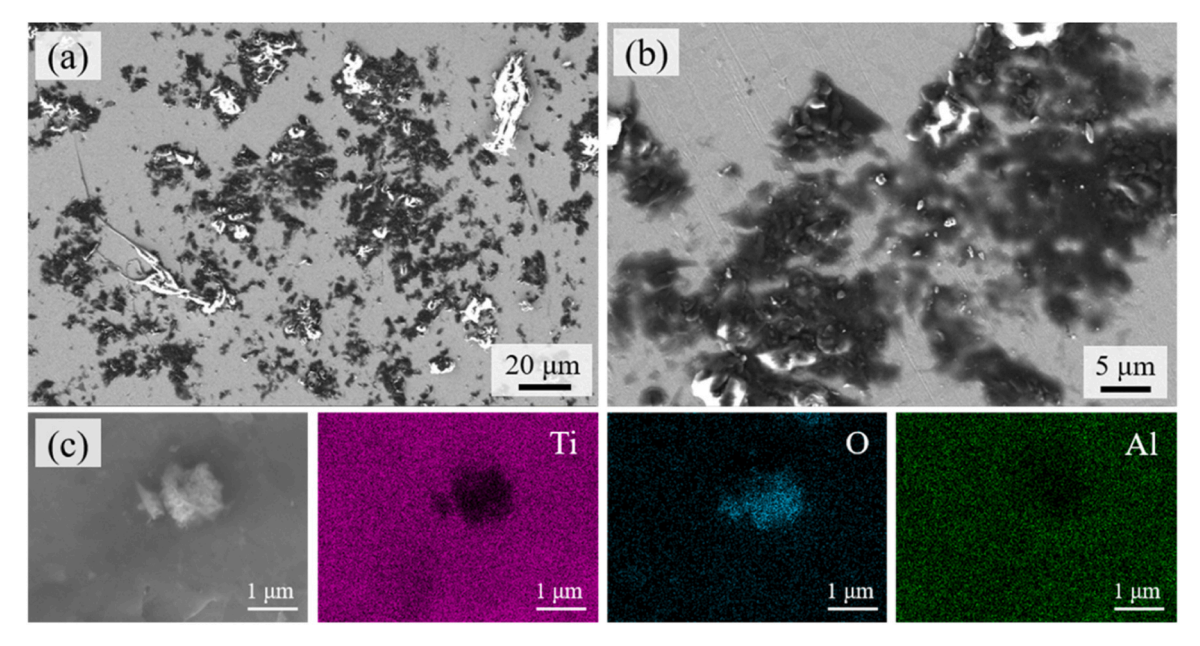


Fig. 11. Morphology of the corroded sample surface after electrochemical measurement (a, b), and (c) the distribution of Ti, O, Al element.

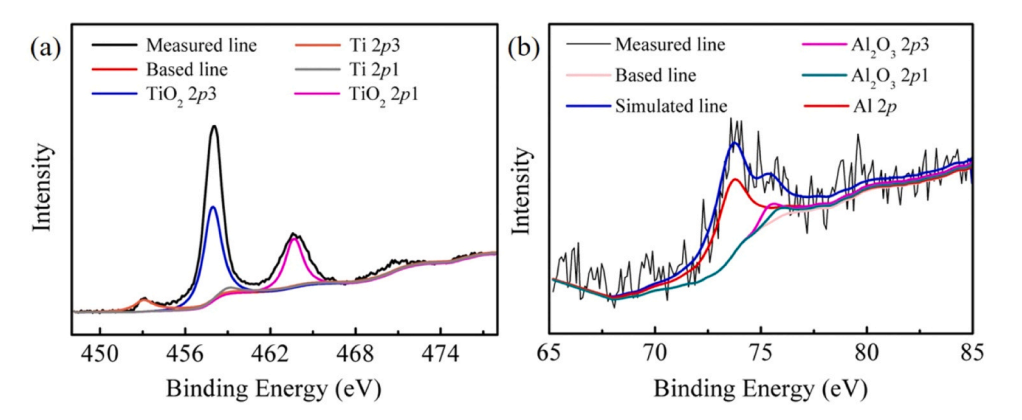


Fig. 12. XPS spectrums of the corroded surface showing the existence of (a) TiO_2 and (b) Al_2O_3 .

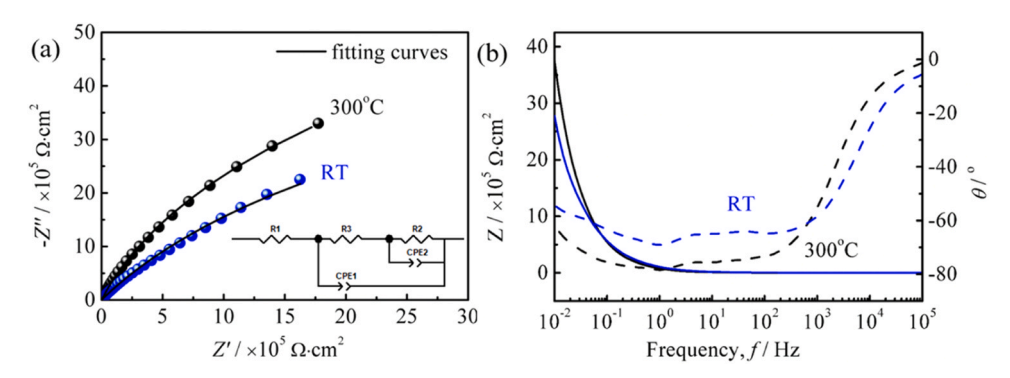


Fig. 13. Nyquist plots of the aged samples and fitting curves (a), and (b) the according Bode and phase diagrams.

[18,32]. Therefore, it is deduced that the α'' decomposition may contribute to ω and O' domains development in this alloy upon aging, and indirectly influences α phase precipitation.

5. Conclusions

In this work a new $(\alpha+\beta)$ Ti alloy is developed, and the influence of intermediate phases transformation during continuous heating on

microstructures as well as properties has been studied. The main conclusions are summarized below:

1) Three intermediate phases are formed in this alloy upon heat treatment, including α'' martensite, O' and ω . During early aging, the α'' martensite decomposes gradually, and the O' and ω are continuously developed. α precipitation takes place at 400 °C.

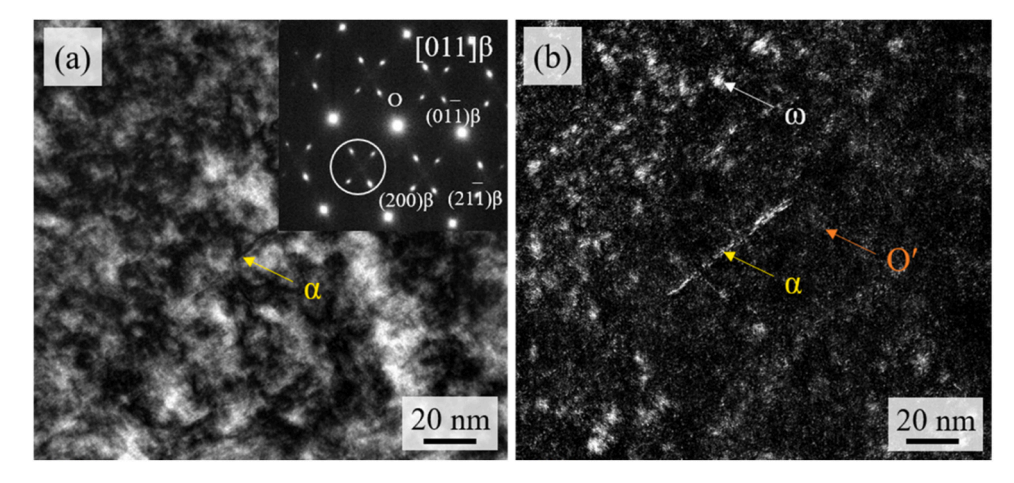


Fig. 14. BFTEM micrograph (a) showing the formation of α needles with the inset SAED pattern along $[011]_{\beta}$ direction, and (b) DFTEM image showing co-existence of α needles, ω and O'.

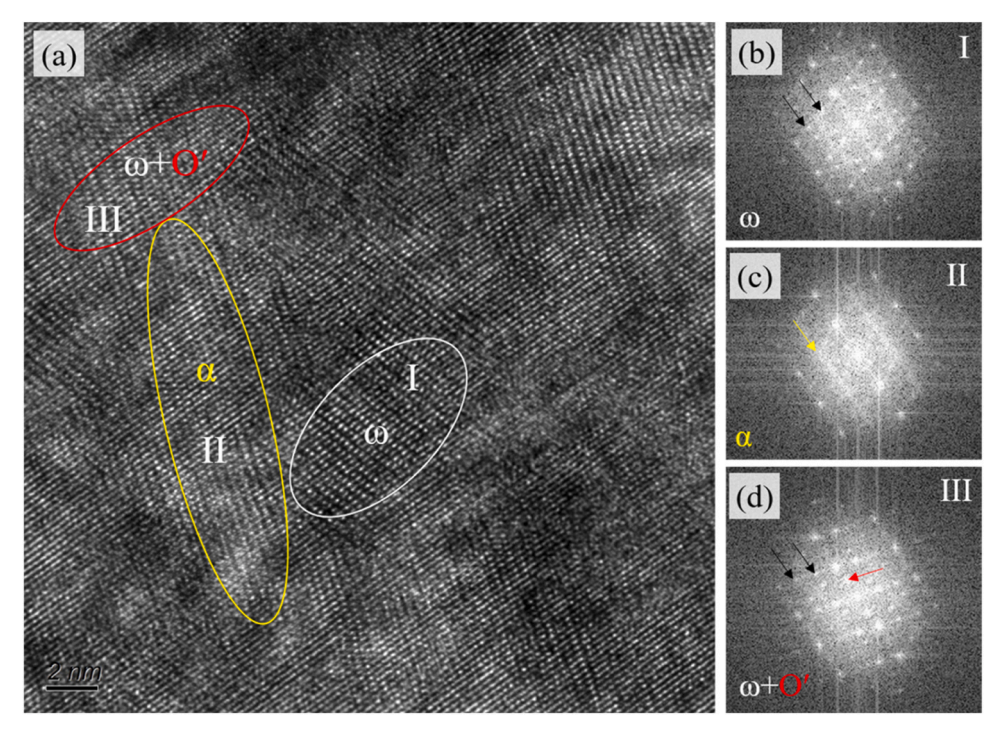


Fig. 15. HRTEM image (a) recorded along $[113]_{\beta}$ directions highlighting the spatial proximity of the α needles, ω and O', and (b-c) FFT micrographs of the regions I, II and III.

- 2) It has been evidenced that the O' and ω precipitates can effectively assist α phase nucleation, and the α tend to nucleate at the boundaries of such two intermediate phases. Even though the α'' martensite decomposes completely before α phase transformation, it is suspected that the α'' martensite plays an indirect role in promoting α precipitation by affecting O' and ω development. Under the mechanism of O' and ω assisting α nucleation, a uniform distribution of fine α precipitates can be obtained.
- 3) Due to finer α precipitates in the sample pre-aged at 300 °C, a comparably higher wear resistance and better anti-corrosion properties are achieved than the other components. Its average friction coefficient and wear ratio are 0.174 and 3.75×10^{-4} mm³/(N·m), respectively. The wear mechanisms of this alloy upon friction test should involve abrasive wear, adhesive wear and oxidation wear. The corrosion current density of this sample in 3.5 wt% NaCl

solution is $1.79\times10^{-8}~\text{A}\cdot\text{cm}^{-2}$. In comparison with that, acceptable corrosion resistance is also obtained in directly aged sample.

CRediT authorship contribution statement

Song Bo: Writing – original draft, Resources, Project administration, Investigation, Funding acquisition. Lian Zhou: Resources, Project administration. Hui Chen: Investigation. Chaoli Ma: Resources, Project administration. Wenlong Xiao: Writing – review & editing, Investigation, Conceptualization. Junshuai Wang: Resources. Yanwei Xue: Investigation. Junjie Ni: Supervision, Investigation.

Declaration of Competing Interest

The authors declare that they have no known competing financial interests or personal relationships that could have appeared to influence

the work reported in this paper.

Data Availability

Data will be made available on request.

Acknowledgments

The authors are grateful to the financial support by the Natural Science Foundation of Shandong Province (No. ZR2022QE115), Liaocheng City Key Research Plan (2022YDSF85), Liaocheng University Doctoral Initiation Fund (318052132), Liaocheng University Students Innovation Plan (CXCY030), National Natural Science Foundation of China (NSFC, Nos. 51671012, 52174346 and 51671007), International Science and Technology Cooperation Program of China (2015DFA51430) and Aeronautical Science Foundation of China (2015ZF51069) to carry out this work.

Appendix A. Supporting information

Supplementary data associated with this article can be found in the online version at doi:10.1016/j.jallcom.2024.176575.

References

- [1] Q.Y. Zhao, Q. Sun, S. Xin, Y. Chen, C. Wu, et al., High-strength titanium alloys for aerospace engineering applications: A review on melting-forging process, Mater. Sci. Eng.: A 845 (2022) 143260.
- [2] S. Shin, C.Y. Zhu, C. Zhang, K.S. Vecchio, Extraordinary strength-ductility synergy in a heterogeneous-structured β-Ti alloy through microstructural optimization, Mater. Res. Lett. 7 (2019) 467–473.
- [3] S. Hu, S. Xiang, Y.B. Tan, W. Shi, Y. Zhang, X.M. Ji, Q. Ran, Synchronous enhancement of the strength and ductility in a metastable β-Ti alloy by a new refined α phase mechanism, J. Alloy. Compd. 922 (2022) 166227.
- [4] Z.H. Zhu, Y.H. Liu, Z.P. Chen, T.Y. Liu, S. Zhang, D.D. Dong, C. Dong, High-strength Ti-Al-V-Zr cast alloys designed using α and β cluster formulas, China Foundry 20 (2023) 23–28.
- [5] Y.F. Xu, H.Q. Liu, S. Zhang, H.Q. Xiong, Effect of duplex aging on microstructural and mechanical behavior of a new β-Ti alloy for biomedical applications, J. Mater. Res. Technol. 18 (2022) 2870–2884.
- [6] S.A. Mantri, D. Choudhuri, T. Alam, et al., Tuning the scale of α precipitates in β-titanium alloys for achieving high strength, Scr. Mater. 154 (2018) 139–144.
- [7] D.D. Li, W.F. Wan, L.Q. Zhu, Y. Jiang, S.Q. Shao, G.J. Yang, H.Q. Liu, D.Q. Yi, S. Cao, Q.M. Hu, Experimental and DFT characterization of interphase boundaries in titanium and the implications for ω-assisted α phase precipitation, Acta Mater. 151 (2018) 406–415.
- [8] Tong Li, Damon Kent, G. Sha, M.S. Dargusch, J.M. Cairney, The mechanism of ω-assisted α phase formation in near β-Ti alloys, Scr. Mater. 104 (2015) 75–78.
- [9] S. Nag, R. Banerjee, R. Srinivasan, J.Y. Hwang, M. Harper, H.L. Fraser, ω-Assisted nucleation and growth of α precipitates in the Ti-5Al-5Mo-5V-3Cr-0.5Fe β titanium alloy, Acta Mater. 57 (2009) 2136–2147.
- [10] Z.Y. Wang, L.B. Liu, D. Wu, L.G. Zhang, W.L. Wang, K.C. Zhou, α'' phase-assisted nucleation to obtain ultrafine α precipitates for designing high-strength near- β titanium alloys, Trans. Nonferrous Met. Soc. China 30 (2020) 2681–2696.
- [11] B. Song, W.L. Xiao, Y. Fu, C.L. Ma, L. Zhou, Role of nanosized intermediate phases on α precipitation in a high-strength near β titanium alloy, Mater. Lett. 275 (2020) 128147.
- [12] S. Antonov, R.P. Shi, D. Li, Z. Kloenne, Y.F. Zheng, H.L. Fraser, D. Raabe, B. Gault, Nucleation and growth of α phase in a metastable β –Titanium Ti-5Al-5Mo- 5 V– 3 Cr

- alloy: Influence from the nano-scale, ordered-orthorhombic O'' phase and α compositional evolution, Scr. Mater. 194 (2021) 113672.
- [13] A. Sharma, V. Soni, S. Dasari, S.A. Mantri, Y.F. Zheng, H. Fraser, R. Banerjee, Fine scale alpha precipitation in Ti-19at%V in the absence of influence from omega precipitates, Scr. Mater. 196 (2021) 113766.
- [14] Yufeng Zheng, R.E.A. Williams, Dong Wang, Rongpei Shi, Soumya Nag, et al., Role of ω phase in the formation of extremely refined intragranular α precipitates in metastable β -titanium alloys, Acta Mater. 103 (2016) 850–858.
- [15] Tong Li, Minjie Lai, A. Kostka, S. Salomon, et al., Composition of the nanosized orthorhombic O' phase and its direct transformation to fine α during ageing in metastable β -Ti alloys, Scr. Mater. 170 (2019) 183–188.
- [16] G.R. Pere Barriobero-Vila, Fernando Warchomicka, Andreas Stark, T.B. Norbert Schell, Phase transformation kinetics during continuous heating of a β-quenched Ti–10V–2Fe–3Al alloy, J. Mater. Sci. 50 (2014) 1412–1426.
- [17] Sang Won Lee, J.M. Oh, Chan Hee Park, J.K. Hong, J.T. Yeom, Deformation mechanism of metastable titanium alloy showing stress-induced α'-Martensitic transformation, J. Alloy Compd. 782 (2019) 427–432.
- [18] Qianglong Liang, Dong Wang, Yufeng Zheng, Shaugnshuagn Zhao, Yipeng Gao, Yulin Hao, Rui Yang, D. Banerjee, H.L. Fraser, Yunzhi Wang, Shuffle-nanodomain regulated strain glass transition in Ti-24Nb-4Zr-8Sn alloy, Acta Mater. 186 (2020) 415-424.
- [19] Bo Song, Yu Chen, Wenlong Xiao, et al., Formation of intermediate phases and their influences on the microstructure of high strength near-β titanium alloy, Mater. Sci. Eng. A 793 (2020) 139886.
- [20] Xiangxing Zhou, Haoyu Fang, Ruidi Li, Tiechui Yuan, Microstructure, mechanical properties and corrosion resistance of low-cost Ti–Al–Cr–Fe alloys processed via powder metallurgy, Mater. Chem. Phys. 317 (2024) 129197.
- [21] J.M. Zadeh, M. Yeganeh, S.R.A. Zaree, M. Khorasanian, Microstructure and corrosion behavior of Ti-10Cu fabricated by selective laser melting, Mater. Today Commun. 39 (2024) 109103.
- [22] Wei Xu, Zhiheng Du, Zhe Wang, Xing Ran, Zhiyong Li, et al., A comparative study on the corrosion, wear, and tribocorrosion performances of Ti-6.5Al-2Zr-1Mo-1V (TA15) alloy fabricated by selective laser melting and laser metal deposition, J. Mater. Res. Technol. 30 (2024) 6245-6253.
- [23] Xian Tong, Q.X. Sun, D.C. Zhang, K. Wang, Y.L. Dai, et al., Impact of scandium on mechanical properties, corrosion behavior, friction and wear performance, and cytotoxicity of a β-type Ti-24Nb-38Zr-2Mo alloy for orthopedic applications, Acta Biomater. 134 (2021) 791–803.
- [24] W. Xu, X. Lu, J. Tian, C. Huang, M. Chen, Y. Yan, L.N. Wang, X.H. Qu, C.E. Wen, Microstructure, wear resistance, and corrosion performance of Ti35Zr28Nb alloy fabricated by powder metallurgy for orthopedic applications, J. Mater. Sci. Technol. 41 (2019) 191–198.
- [25] J.J. Oak, D.V. Louzguine-Luzgin, A. Inoue, Synthetic relationship between titanium and alloying elements in designing Ni-free Ti-based bulk metallic glass alloys, Appl. Phys. Lett. 91 (2007) 053106.
- [26] M.J. Lai, C.C. Tasan, J. Zhang, B. Grabowski, L.F. Huang, D. Raabe, Origin of shear induced β to ω transition in Ti–Nb-based alloys, Acta Mater. 92 (2015) 55–63.
- [27] Yufeng Zheng, R.E.A. Williams, S. Nag, R. Banerjee, H.L. Fraser, D. Banerjee, The effect of alloy composition on instabilities in the β phase of titanium alloys, Scr. Mater. 116 (2016) 49–52.
- [28] P. Siahpour, S.M.T. Omar, D. Griffin, M.Y. Amegadzie, A. Tieu, I.W. Donaldson, K. P. Plucknett, Evaluating surface mechanical properties and wear resistance of Ti–6Al–4V alloy subjected to ultrasonic pulsed waterjet peening, Wear 550-551 (2024) 205400.
- [29] Q. Zhao, Y. Pan, Y.G. Zhang, C.X. Wang, G.J. Zhang, Effect of phase composition on the corrosion behavior of Ti-xMo alloy films, Surf. Coat. Technol. 484 (2024) 130838.
- [30] L.X. Zhang, Z.S. Wu, Y. Li, Y.L. Feng, F. Zhao, Study on microstructure, mechanical and corrosion behavior of Ti-6Al-4V titanium alloy by Keyhole gas tungsten arc welding, Mater. Today Commun. 40 (2024) 109530.
- [31] V.B.O. Pere Barriobero-Vila, Sabine Schwarz, Thomas Buslaps, Guillermo Requena, Tracking the α" martensite decomposition during continuous heating of a Ti-6Al-⁶V-²Sn alloy, Acta Mater. 135 (2017) 132–143.
- [32] Q.L. Liang, Z. Kloenne, Y.F. Zheng, D. Wang, S. Antonov, Yipeng Gao, Yulin Hao, Rui Yang, Yunzhi Wang, H.L. Fraser, The role of nano-scaled structural non-uniformities on deformation twinning and stress-induced transformation in a cold rolled multifunctional β -titanium alloy, Scr. Mater. 177 (2020) 181–185.